Chemical Engineering Journal 454 (2023) 139986

Contents lists available at ScienceDirect

Chemical Engineering Journal

journal homepage: www.elsevier.com/locate/cej

Engineering manganese-rich phospho-olivine cathode materials with exposed crystal {010} facets for practical Li-ion batteries

Shaojun Liu [a], Jingang Zheng [a], Bo Zhang [b], Yingqiang Wu [b,*], Jinli Liu [b,d], Lianfang Yin [b], Miao Zhan [a], Yuanhua Xiao [c], Baigang An [a], Li Wang [b], Chengguo Sun [a,d,*], Xiangming He [b,*]

[a] School of Chemical Engineering, University of Science and Technology Liaoning, Anshan 114051, PR China
[b] Institute of Nuclear and New Energy Technology, Tsinghua University, Beijing 100084, PR China
[c] Zhengzhou University of Light Industry, College of Materials and Chemical Engineering, Zhengzhou 450002, PR China
[d] China National Quality Supervision and Inspection Center for Industrial Explosive Materials, Nanjing University of Science and Technology, Nanjing 210094, PR China

ARTICLE INFO

Keywords:
Manganese-rich olivine
Crystal orientation
Cobalt doping
Kinetic property
Commercialization

ABSTRACT

Manganese-rich $LiMn_{1-y}Fe_yPO_4$ (e.g., $LiMn_{0.7}Fe_{0.3}PO_4$) is emerging as the most promising olivine cathode material after $LiFePO_4$, which has a current market demand of >500000 tons per year. However, its commercial application is challenging because of its poor kinetic properties. Although nanocrystallization is a transformative paradigm for improving the kinetics, it results in the concomitant problem of increasing the specific surface area of the material, which leads to more interfacial side reactions. Here, we develop a polyol solvothermal method to boost the particle size (decrease the specific surface area) whilst simultaneously regulating the crystal orientation (improving the kinetics) of $LiMn_{0.7}Fe_{0.3}PO_4$. Importantly, the synthesis can be used at the ton scale, with the offtake potential reaching 1000 tons per year. Cobalt doping and carbon coating are combined to further increase the kinetic properties. Electrochemical measurements demonstrate that the diffusion of the Li^+ kinetics is increased by 58.6 % and 46.1 % for the $Fe^{2+/3+}$ and $Mn^{2+/3+}$ redox couple during charging and 92.0 % and 21.2 % during discharging, respectively. A capacity of 150 mAh g^{-1} at a 5C rate is then delivered. In full batteries (14000 mAh), the capacity retention reaches 89.6 % over 1000 cycles at a 1C rate.

1. Introduction

As a cathode material with significant advantages regarding high safety and low toxicity and cost [1–5], olivine $LiFePO_4$ has been one of the most important cathode materials in the lithium-ion batteries (LIBs) industry. However, the energy density of $LiFePO_4$ batteries is encountering a bottleneck due to the low working voltage (3.4 V vs Li/Li^+) and theoretical capacity of 170 mAh g^{-1} of the $LiFePO_4$ cathode [6]. Utilizing the olivine frameworks, one method to increase the energy density is to replace Fe with Mn (i.e., $LiMnPO_4$). The unique electronic structure of Mn^{2+} in olivine frameworks and the induced effect of a strong P—O bond in Mn—O—P lead to the working voltage of the $Mn^{3+/2+}$ couple reaching ~4.1 V (vs Li/Li^+) [7–11] and a theoretical energy density of ~700 Wh kg^{-1} (21 % higher than that of $LiFePO_4$) [12].

However, the commercial application of $LiMnPO_4$ is challenging because it suffers from much lower electronic conductivity and Li^+ diffusivity compared with $LiFePO_4$ [13,14]. The slow kinetics come from the intrinsic aspects of the solid $LiMnPO_4$ material, especially its crystallographic and transport properties [15]. In the crystal structure of $LiMnPO_4$, the MnO_6 octahedron is isolated by the PO_4 tetrahedron. The strong P—O covalent bonds prevent Li^+ from passing through the PO_4^{3-} tetrahedron site so that the Li^+ can only transport in one-dimensional diffusion along the *b*-axis [16,17]. Furthermore, the delithiation and lithiation of $LiMnPO_4/MnPO_4$ undergo a two-phase mechanism, where the large lattice mismatch between the $LiMnPO_4$ and $MnPO_4$ phases not only presents a large energy barrier for Li^+ diffusion across the phase boundary but also increases the barrier for the electron transition [18–20]. This is attributed to the electron lattice interaction around Mn^{3+} ions, whose large Jahn–Teller effect strongly binds polaron holes and increases the effective mass of polarons rapidly [15,21,22]. The large effective mass of the polarons around the Mn^{3+} sites coupled with large local lattice deformations induce slow kinetics and internal friction, either in the bulk crystal or at the mismatched $LiMnPO_4/MnPO_4$ two-phase interface, which easily blocks the one-dimensional lithium-ion path [20].

In this context, the partial substitution of Mn^{2+} by Fe^{2+} to form

* Corresponding authors.
E-mail addresses: yqwu02@tsinghua.edu.cn (Y. Wu), sunyangguo2004@163.com (C. Sun), hexm@tsinghua.edu.cn (X. He).

https://doi.org/10.1016/j.cej.2022.139986
Received 27 July 2022; Received in revised form 7 October 2022; Accepted 14 October 2022
Available online 26 October 2022

$LiMn_{1-y}Fe_yPO_4$ (e.g., $LiMn_{0.7}Fe_{0.3}PO_4$) has been proposed. Ab initio calculations have confirmed that Fe substitution can increase the solubility limits of $LiMn_{1-y}Fe_yPO_4$ and $Mn_{1-y}Fe_yPO_4$ in each other, resulting in an expanded single-phase region and a contracted two-phase region [23]. The size of the single-phase region depends on the Fe content, where the range of the solid solution is widest when the Fe content is~0.3 [18]. Thus, the bulk kinetic behavior of $LiMn_{0.7}Fe_{0.3}PO_4$ is improved by reducing the hindrance of electronic transport by expanding the single-phase solid solution reaction area and introducing dopants [24–26]. Other strategies, including reducing lattice distortion [27–30], reasonably controlling the defect concentration [31–34] and designing an appropriate particle morphology [35,36], have also been considered.

Among these strategies, nanocrystallization represents a transformative paradigm for improving the kinetic properties of $LiMn_{0.7}Fe_{0.3}PO_4$. This is because it can effectively shorten the diffusion length of Li^+ ions across the crystal. However, a concomitant challenge for this method is the resulting high specific surface area of the materials, which leads to more interfacial side reactions, the dissolution of Mn ions and battery decay [37,38]. In addition, the lower compaction density of the electrode due to nanocrystallization will decrease the energy density of the battery. Our previous studies have demonstrated that the crystal orientation of $LiFePO_4$ nanoplates (i.e., *ac* or *bc* facet) can be regulated by the mixing procedure of starting materials in the glycol-based solvothermal process [39]. $LiFePO_4$ nanoplates with a crystal orientation along the *ac* facet deliver superior rate performance than that of the sample with *bc* facet due to the shorter diffusion distance of Li^+ along the *b* direction. This strategy offers an ideal opportunity to enable high kinetics whilst simultaneously boosting the particle size of $LiMn_{0.7}Fe_{0.3}PO_4$.

In this work, we develop a polyol solvothermal method to boost the particle size (decrease the specific surface area) of $LiMn_{0.7}Fe_{0.3}PO_4$, by which the crystal orientation is regulated to make it grow along with the *ac* facet [40–43]. The purpose is to shorten the diffusion distance of Li^+ along the *b* direction when the particle size being regulated to lower the specific surface area of the material. Then, Cobalt doping and carbon coating are then combined to further increase the kinetics. The synthesis processes are investigated at the ton scale to evaluate their commercialization potential. Furthermore, the electrochemistry of the as-obtained $LiMn_{0.7}Fe_{0.3}PO_4$, including the cycling and rate performance, kinetics and long lifetime testing in a pouch cell, is assessed. Finally, first-principles calculations are conducted to reveal the reasons for the improved electrochemical performance.

2. Experimental

2.1. Materials and synthesis

The raw materials, including $LiOH{\cdot}H_2O$, H_3PO_4 (85 wt%), $MnCl_2{\cdot}4H_2O$, $FeSO_4{\cdot}7H_2O$, $CoSO_4{\cdot}7H_2O$ and glycol were purchased from Sinopharm Chemical Reagent Co., Ltd., China and were of analytical purity. In the synthesis process, the molar ratio of $LiOH{\cdot}H_2O$, $MnCl_2{\cdot}4H_2O$, $FeSO_4{\cdot}7H_2O$ and H_3PO_4 was set as 3:0.7:0.3:1, respectively. For the Co-doped sample, the Co was designed to replace the Mn site, where the molar ratio of $LiOH{\cdot}H_2O$, $MnCl_2{\cdot}4H_2O$, $CoSO_4{\cdot}7H_2O$, $FeSO_4{\cdot}7H_2O$ and H_3PO_4 was set as 3:0.69:0.1:0.3:1 in the feeding process. The pristine sample was labeled as LMFP. The Co-doped sample was labeled with the doping content, e.g., LMFP-1 %Co for a Co-doping content of 1 %Co was easy doped into the crystal lattice of $LiMn_{0.7}Fe_{0.3}PO_4$. The inductively coupled plasma optical emission spectroscopy (ICP-OES) measurements showed that the Co content was 0.97 %.

For the synthesis of pristine $LiMn_{0.7}Fe_{0.3}PO_4$, typically, 15 mmol $FeSO_4{\cdot}7H_2O$, 35 mmol $MnCl_2{\cdot}4H_2O$ and 80 mL of glycol were mixed to form solution A. Next, 150 mmol of $LiOH{\cdot}H_2O$ was solved in 80 mL of glycol to form solution B. Under stirring, 50 mmol of H_3PO_4 was added to B solution to form solution C, which was added into solution A dropwise. After 10 min of stirring, the mixed solution was transferred into an autoclave (200 mL) and then heated at 180–235 °C for various times (Note: the solvent would be carbonized when the heated temperature beyond 240 °C, leading to a big challenge for the recycling of the glycol). The reaction temperature and time were controlled to increase the particle sizes and decrease the specific surface area of the productions. After the reaction, the cooled solution was filtrated and washed with water five times (Note: the residual LiOH can be recycled as Li_2SO_4, while glycol could be recycled by almost 100 % in the process engineering). A scale-up experiment at the ton scale was accessed (Fig. S1). For the carbon coating, 90 wt% pristine $LiMn_{0.7}Fe_{0.3}PO_4$ and 10 wt% sucrose were dispersed in water to form a solution and then spray dried to prepare spherical particles. These dried powders were sintered for 4 h at 700 °C under an N_2 atmosphere [36,44,45].

2.2. Characterization

XRD data were collected using a powder X-ray diffractometer (Bruker AXS D8 Advance) with Cu K_α radiation ($\lambda = 1.5406$ Å) in the 2θ range of 10°–90°. The morphology of the LMFP powder and the EDS mapping of the Mn, Fe and C elements were analyzed by scanning electron microscopy (Thermofisher Apreos), while their structural characteristics were observed via transmission electron microscopy (JEM-2100, 200 kV). The contents of Mn, Fe and Co in the materials were analyzed using ICP-OES. BET data were collected with a Micromeritics ASAP 2420.

2.3. Electrode preparation and electrochemistry

The LMFP powders, conductive materials (C45) and poly(vinylidene fluoride) (Solef 5130) were mixed with a weight ratio of 93:3:4 in *N*-methyl pyrrolidinone. They were well mixed to obtain a slurry, which was then coated on an aluminum foil and dried in a vacuum for 10 h at 120 °C. For the 2032-type coin battery, the electrode was cut into a wafer with a diameter of 12 mm, where the active mass loading was ~9.8 mg cm^{-2}. The battery was assembled in an argon-filled glovebox (the contents of O_2 and H_2O were maintained below 0.1 ppm) using a Celgard 2400 separator and electrolyte of 1 mol/L $LiPF_6$ in EC + DMC. Charge-discharge cycling tests of the Li || LMFP half-cell were carried out in constant-current mode in the range of 2.0–4.5 V at 0.1C (1C = 170 mA g^{-1}). For the pouch cell, the capacity of the battery was ~14000 mAh with graphite as the negative electrode and the assembly carried out by Harbin Guangyu New Energy Co., Ltd., China. The galvanostatic charge/discharge curves were recorded using a LANHE instrument. Electrochemical impedance spectroscopy (EIS) measurements were determined using a Zahner electrochemical workstation with a frequency range of 0.01–100 kHz.

3. Results and discussion

The SEM image of the LMFP prepared for 8 h at 180 °C is shown in Fig. S2**a**. The sample presents the morphology of a monodisperse nanoplate with an average particle size of ~80 nm (Fig. S2**b**). Fig. 1**a** and Fig. S3**a** show the SEM image and corresponding size distribution of the Co-doped sample (LMFP-1 %Co) produced with the same reaction conditions as LMFP, respectively. Although Co doping does not change the particle morphology and crystal size (also~80 nm), the lattice parameters decreased after the doping (Table S1), which demonstrated that Co substituted apparently into the octahedral 4c site of Fe or Mn, which might reduce the Li/Fe cation mixing in the lattice and then increased the kinetics of the sample compared with that of the LMFP (Fig. S8) [46]. However, the specific surface area of this LMFP-1 %Co sample reaches as high as 34.0 m^2/g (Fig. S3**d**), which gives rise to significant difficulty in the electrode process, such as the powders falling off the electrode during cutting (Fig. S2**c**). To decrease the specific surface area (or boost the particle size), the reaction temperature is

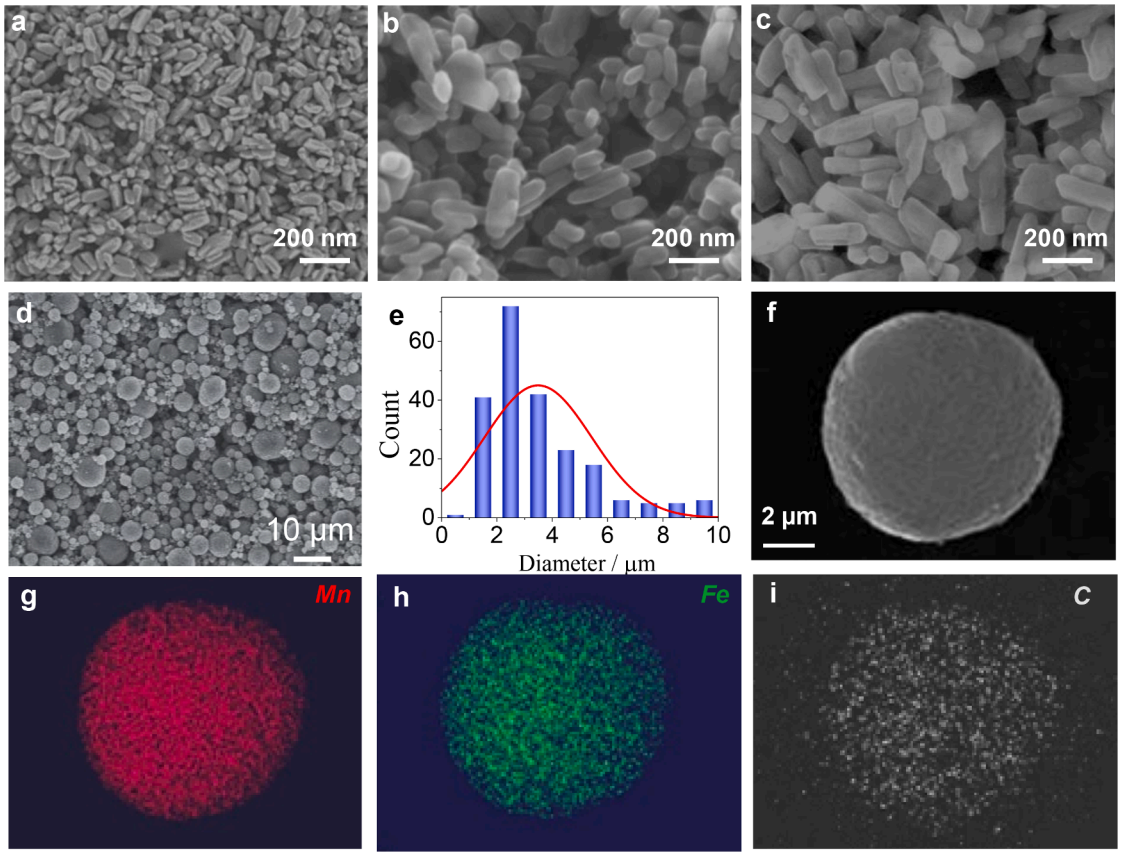

Fig. 1. Characterizations of the LMFP-1 %Co materials. SEM images of LMFP-1 %Co from various solvothermal process conditions: (a) 8 h at 180 °C, (b) 16 h at 210 °C, and (c) 24 h at 235 °C. (d) SEM image and (e) particle size distribution of LMFP-1 %Co after spray drying. EDS mapping of (g) Mn, (h) Fe, and (i) C elements in the spheroidal particle.

increased to 210 °C for 16 h. It is shown that the particle size of the sample is increased to~160 nm (Figs. 1**b and** S3**b**) and the corresponding specific surface area decreased to 18.7 m^2/g (Fig. S3**e**). Considering the balance between particle size and specific surface area, an average particle size of ~245 nm (Fig. 1**c and** S3**c**) and a specific surface area of 14.8 m^2/g (Fig. S3**f**) are finally accessed when the reaction temperature is set for 24 h at 235 °C.

For the carbon coating, a spray drying technology is applied. After the drying, a uniform microsphere morphology with an average particle size of ~4 μm is successfully prepared (Fig. 1**d and e**). The EDS mapping images further demonstrate that the Mn, Fe and C elements are distributed homogeneously in the sphere in Fig. 1**f–i**. HR-TEM demonstrates that the carbon coating layer is ~2–3 nm (the total carbon content is ~2 wt%) (Fig. 2**a and b**).

The TEM images also show the monodisperse nanoplate structure of the LMFP and LMFP-1 %Co samples (Fig. S4). The XRD plots further confirm the crystal growth orientations along the *ac* facet (Fig. 2**d and e**). First, the diffraction peaks of the samples are sharp and symmetric, which can be indexed to pure $Li(Mn,Fe)PO_4$ (No. 89–7115) and belong to the Pmnb (62) space group. Second, the intensity ratio of $I_{(020)}/I_{(200)}$ of LFMP and LFMP-1 %Co reaches 2.578 and 2.558 (Fig. 2**e**), respectively, implying the *ac*-facet plate morphology of both samples [39,47]. More evidence of the preferred orientation is presented in the HR-TEM characterization (Fig. 2**a–c**). The clear lattice fringe indicates the high crystallinity of the samples. The diffraction spots demonstrate that the exposed crystal facet of both samples is (0 1 0), which is perpendicular to the (1 0 1) and (2 0 1) facets (Fig. 2**c**).

Fig. S5**a** compares the charge and discharge curves of the LMFP and LMFP-1 %Co samples with the specific surface area of 18.7 m^2/g under a 0.1 C rate. The two platforms of 4.1 and 3.5 V (vs Li/Li^+) belong to the electrochemical redox of the $Mn^{2+/3+}$ and $Fe^{2+/3+}$ couples (Fig. 3**a and b**), respectively. The LMFP cell delivers a capacity of 150.5 mAh g^{-1}, of which the 4.1 V platform ($Mn^{2+/3+}$ redox couple) contributes 94.8 mAh g^{-1} (Fig. S5**a**). This long platform of the $Mn^{2+/3+}$ redox couple demonstrates that the kinetics of Li^+ are improved due to the special crystal orientation (i.e., *ac* facet) and the uniform carbon coating. Furthermore, the LMFP-1 %Co presents higher discharge capacities of ~165.7 and ~102.0 mAh g^{-1} for the $Mn^{2+/3+}$ platform capacity, which are 15.2 (total capacity) and 7.2 mAh g^{-1} ($Mn^{2+/3+}$ platform) higher than that of the LMFP sample. These results imply that the Co doping can also improve the kinetics of Li^+ and then the capacitive properties. The normalized curves in Fig. 3**a and b** demonstrate that the polarization of the LMFP-1 %Co cell is decreased after Co doping. Fig. 3**c** compares the cycling performances of the LMFP and LMFP-1 %Co samples at a 1C rate. After 250 cycles, the capacity of the LMFP-1 %Co sample is maintained at 148.5 mAh g^{-1}, which is 20.6 mAh g^{-1} higher than that of the LMFP sample. A longer cycle test for the LMFP-1 %Co sample is shown in Fig. S6, where the discharge capacity is maintained at 132 mAh g^{-1} with a capacity retention of 88.6 % after 1000 cycles.

The rate performances of the LMFP and LMFP-1 %Co are shown in Fig. 3**d to f**. The capacity of the LMFP sample at 0.1, 1, 5 and 10C is 152, 136, 124 and 117 mAh g^{-1} (Fig. 3**d**), respectively. For the LMFP-1 %Co sample, the rate performance improves significantly due to the better Li^+ kinetics. The capacity at 0.1, 1, 5 and 10C is 165, 154, 150 and 147 mAh g^{-1} (Fig. 3**e**), respectively. The rate performances of the LMFP with various Co doping content are shown in Fig. S8. Comparing with the pristine LMFP, the capacity could be increased 15.1 %, 25.1 %, and 13.4 % at 10C-rate when the doping content was 0.5 %, 1 %, and 2 %, respectively. Besides, the doping of Co presented better rate performance than other dopants, such as Mg [48], Ni [49], and Ti [50]

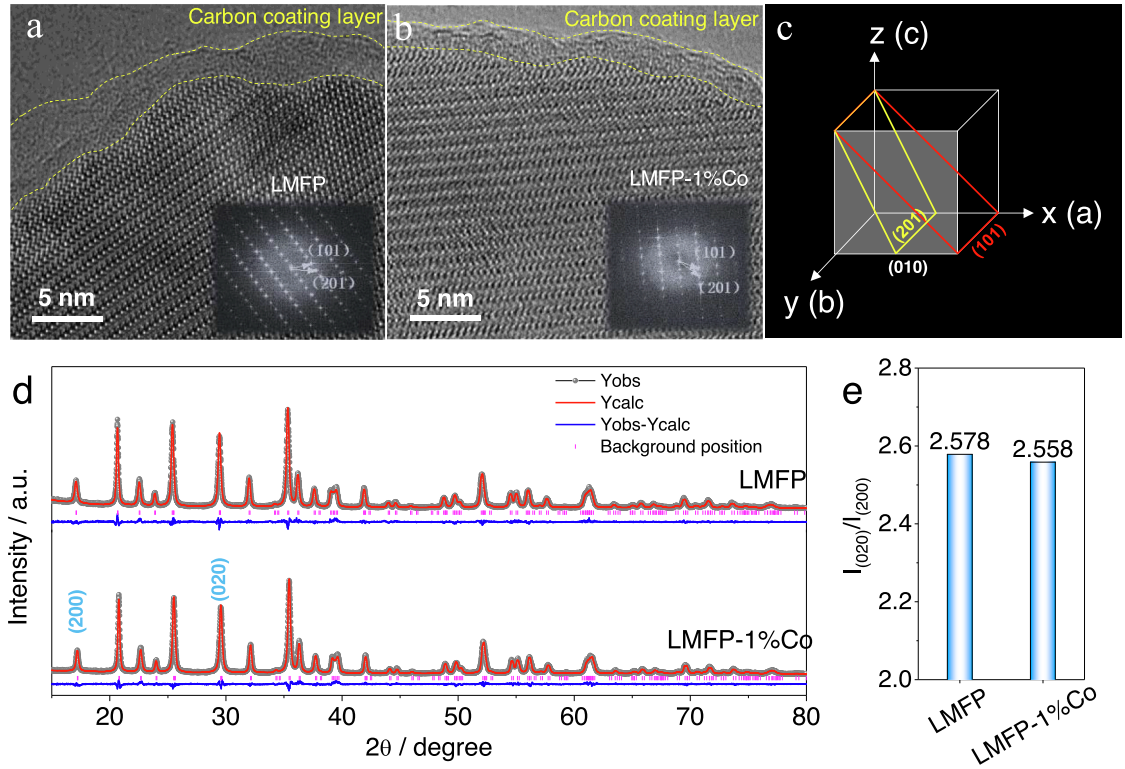

Fig. 2. Characterizations of the crystal orientation and surface carbon coating layer. HR-TEM images of (a) LMFP and (b) LMFP-1%Co. (c) Exposure facet for both samples is confirmed as (0 1 0) by SAED (insets of (a) and (b)). (d) XRD patterns of LMFP and LMFP-1%Co and (e) intensity ratio of $I_{(020)}/I_{(200)}$ of XRD.

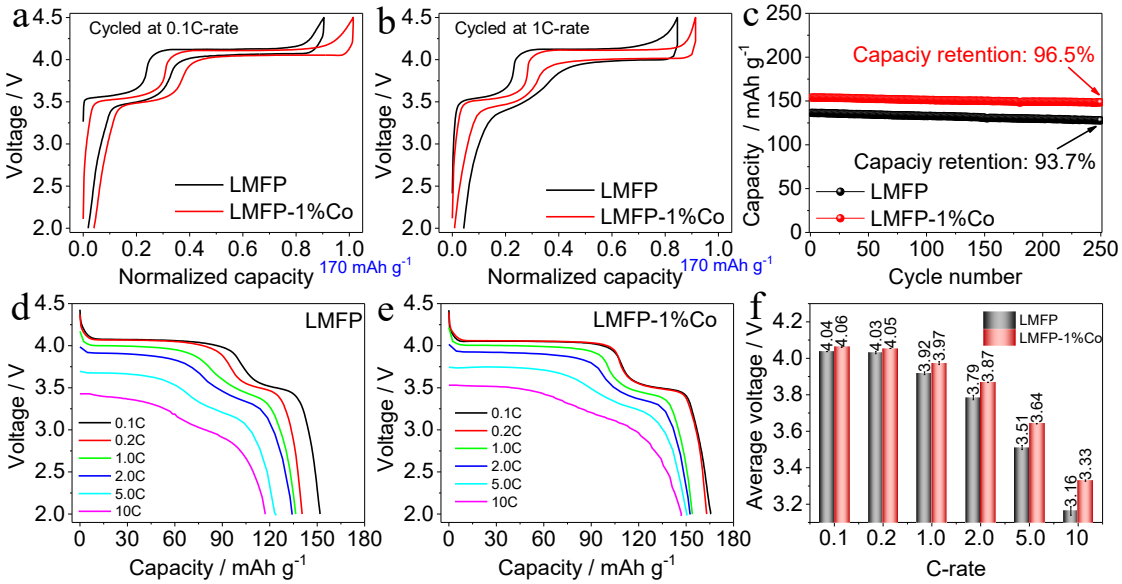

Fig. 3. Electrochemical performance of coin cells. Charge-discharge profiles of batteries cycled at (a) 0.1C and (b) 1C. (c) Cycling performance of LMFP and LMFP-1%Co at 1C. Discharge curves of (d) LMFP and (e) LMFP-1%Co at various C-rates. (f) Average discharge voltage under various C-rate.

(Table S2). Fig. 3**f** compares the average voltage of the LMFP and LMFP-1 %Co samples during rate discharge, in which the discharge voltage of the LMFP-1 %Co is higher than that of the LMFP and an obvious difference enlarges with the increased C-rate. The results are consistent with the above conclusion that Co doping improves the kinetics of Li^+.

A pouch cell is then used to evaluate the performances of the LMFP-1 %Co in a practical battery, where graphite is used as the negative electrode and the N/P ratio is set as 1.1 (Fig. 4**a**). The capacity of the battery is ~14000 mAh and it was assembled by Harbin Guangyu New Energy Co., Ltd., China. Fig. 4**b and c** present the long cycling performance of the battery under a 1C rate charge and discharge at room temperature. The battery can deliver an initial capacity of ~13500 mAh. After 1000 cycles, the capacity is maintained at ~12100 mAh, where the capacity retention is 89.6 % (Fig. 4**c**). Fig. 4**d** shows the dQ/dV curves of the battery during the cycling, where the high coincidence of the curves indicates the high structural stability of the LMFP-1 %Co during charge

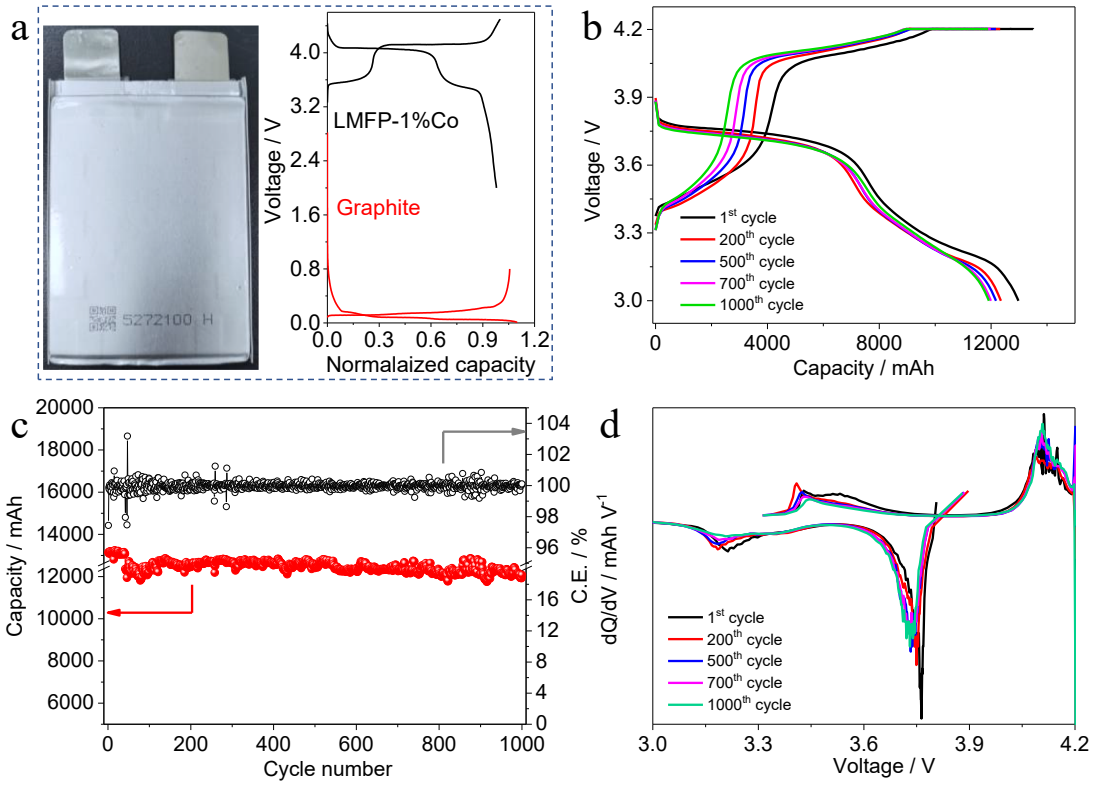

Fig. 4. Electrochemical performance of pouch cell. (a) Photograph of pouch cell and graphic illustration of the N/P ratio. (b) Charge and discharge curves of pouch cell under 1C (14000 mA). (c) Long cycling performance and Coulombic efficiency and (d) dQ/dV curves of battery during cycling.

and discharge cycling.

The above characterization of the morphology and crystal structure and electrochemical performance measurements demonstrate the significant advantages of controlling the crystal orientation and particle size. The as-obtained LMFP-1 %Co sample exhibits substantial potential in the application of high-energy LIBs. To understand the improved performance after Co doping, the kinetics of Li^+ are investigated by cyclic voltammetry (CV) (Fig. 5**a and b**). The linear relationship between the peak current (i_p) and the square root of the scanning rate ($\upsilon^{1/2}$) in Fig. 5**c and d** illustrates a typical diffusion-controlled response. Based on the Randles–Sevcik equation, $i_p = 268600n^{2/3}SD1^{/2}C\upsilon^{1/2}$, where n is the charge transfer number, C is the concentration (mol cm^{-3}) and S is the surface area of the electrode. We can calculate the apparent chemical diffusion coefficients of lithium ions (i.e., D_{Li}) from the slope of $di/d\upsilon^{1/2}$. Before the calculation, we need to presume that the apparent D_{Li} values are constant in the whole phase transition regime and the system is regarded as a homogeneous system. In this case, it should be more reasonable to present the relative increased value by the slope of $di/d\upsilon^{1/2}$. This is because a consistent electrode can be guaranteed by the electrode preparation technology, while the absolute values of S and C in the Randles–Sevcik equation are difficult to accurately obtain at a powder electrode level.

Fig. 5**c and d** compare the kinetics of Li^+ for the $Fe^{2+/3+}$ and $Mn^{2+/3+}$ couples during charge and discharge, respectively. After Co doping (i.e., LMFP-1 %Co), the kinetics of Li^+ are increased by 58.6 % and 46.1 % for the $Fe^{2+/3+}$ and $Mn^{2+/3+}$ couples during charging, while the corresponding values are 92.0 % and 21.2 % during discharging, respectively. These results explain the improved polarization and rate performances after Co doping (Fig. 3). The electrochemical impedances under the different charges of state (SOC) are shown in Fig. S7. Consistently, the impedances under 30 % and 80 % SOC are decreased by ~15.7 % (from 98.1 to 82.7 Ohm) and ~11.0 % (from 96.1 to 86.5 Ohm), respectively. The characterizations of the LMFP-1 %Co sample before and after 100 cycles by XRD and XPS are shown in Fig. S9, which further demonstrated the structure of the LMFP-1 %Co could maintain stability during charge/discharge cycling. First-principles calculations are also conducted to reveal the reasons for the improved electrochemical performance. Considering that the advantageous crystal facet of LMFP-1 %Co is the *ac* facet, a comparative study of the Mn dissolution at the *ac* and *bc* facets under 0 % SOC and 100 % SOC is conducted, respectively (Fig. 5**e**). The results show that the energy needed for the dissolution of Mn ions from the *ac* facet is 8.95 and 7.92 eV under 0 % SOC and 100 % SOC (Fig. 5**f**), respectively, while the value for the *bc* facet is 7.35 and 5.09 eV, respectively. Therefore, Mn ions are more difficult to be dissolved from the *ac* crystal facet of the crystal, resulting in the long lifespan of practical LIBs using the LMFP-1 %Co cathode material.

4. Conclusions

In summary, the purpose of this work was to resolve the issues of $LiMn_{0.7}Fe_{0.3}PO_4$ cathode materials, particularly the concomitant problems of the high specific surface area during nanocrystallization and their engineering for ton-scale synthesis. High-quality $LiMn_{0.7}Fe_{0.3}PO_4$ cathode materials have been successfully synthesized by a polyol solvothermal method and the synthesis has been addressed up to the ton scale with an off-take potential reaching 1000 tons per year. The particle size of the $LiMn_{0.7}Fe_{0.3}PO_4$ was boosted to ~245 nm and the corresponding specific surface area was reduced to 14.8 m^2/g. The crystal orientation was also well regulated to make it grow along with the *ac* facet. Furthermore, cobalt doping and carbon coating have been successfully conducted to increase the diffusion of the Li^+ kinetics. Hence, the LMFP-1 %Co sample presented preferable electrochemical performances comparing with pure $LiFePO_4$ and $LiMnPO_4$ baseline (Table S2).

Electrochemical measurements demonstrate that the diffusion of the Li^+ kinetics was increased by 58.6 % and 46.1 % for the $Fe^{2+/3+}$ and $Mn^{2+/3+}$ couples during charging and 92.0 % and 21.2 % during discharging, respectively. First-principles calculations further confirmed that the Mn ions are more difficult to be dissolved from the *ac* facet of the

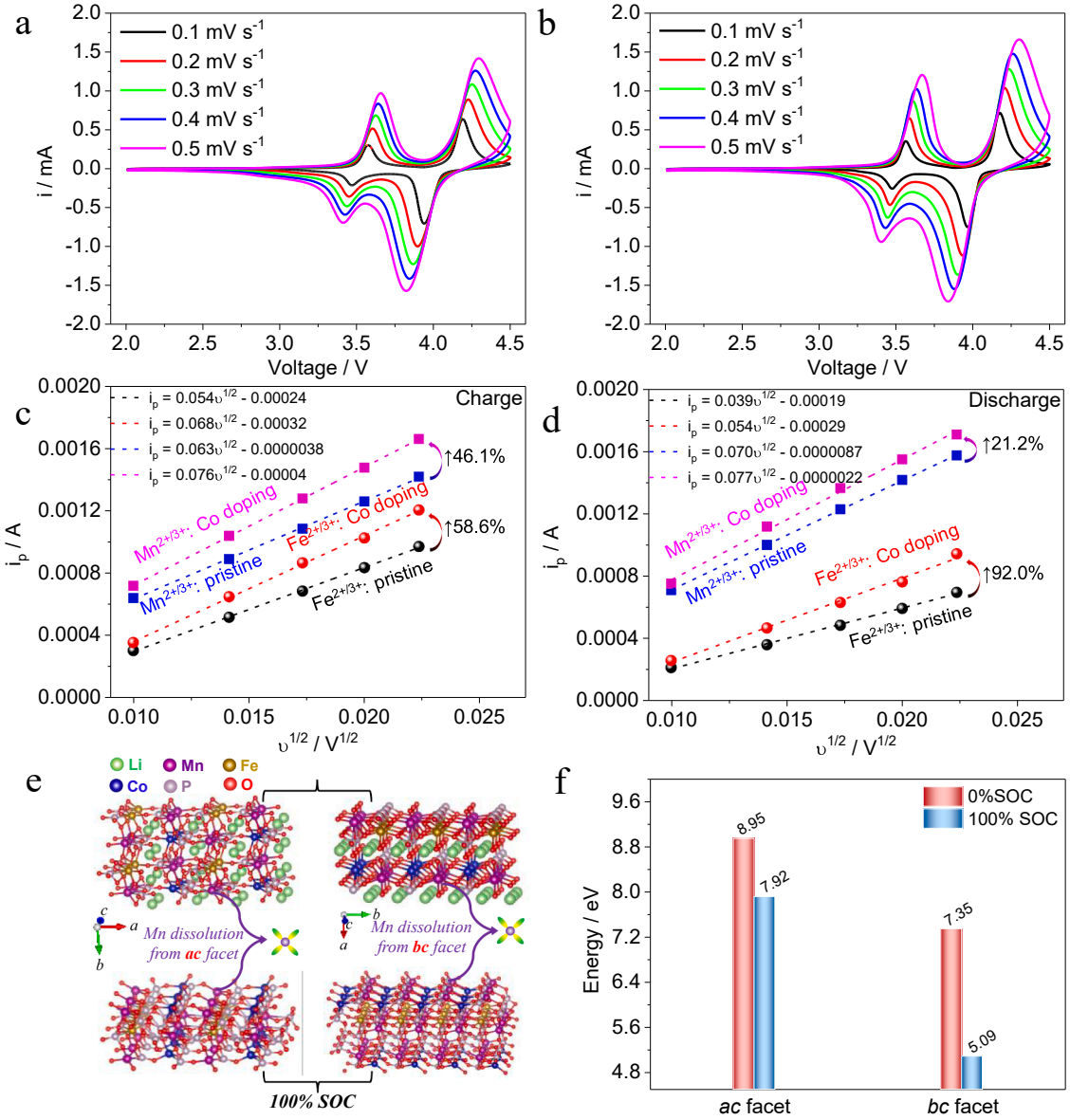

Fig. 5. Analysis of diffusion kinetics and first-principles calculations. CV curves of (a) LMFP and (b) LMFP-1 %Co at various sweep rates. Kinetics of Li^+ calculated by Randles–Sevcik equation based on CV curves during (c) charge and (d) discharge. (e) Graphic illustration of Mn ions dissolved from *ac* and *bc* facets at 100 % and 0 % SOC, where the green, purple, golden, blue, red, and purple gray ball refer to Li, Mn, Fe, Co, O, and P atom, respectively. (f) Energy needed for dissolution of Mn ions from *ac* and *bc* facets.

crystal. Because of these positive effects, a capacity of 150 mAh g^{-1} at a 5C rate was obtained. In full batteries (14000 mAh), the capacity retention reached 89.6 % over 1000 cycles at a 1C rate.

Author Contributions.

S.J. Liu, J.G. Zheng, J.L. Liu, and L.F. Yin synthesized and characterized the materials, and carried out the electrochemical tests. B. Zhang performed the First-principles calculations. Y.Q. Wu and S.J. Liu wrote the manuscript with input from all authors. All authors reviewed and approved the final version of the manuscript.

Declaration of Competing Interest

The authors declare that they have no known competing financial interests or personal relationships that could have appeared to influence the work reported in this paper.

Data availability

Data will be made available on request.

Acknowledgments

We would like to show gratitude to the National Natural Science Foundation of China (Nos. 22279071, 11972178, 51972156 and U21A20170) and the Ministry of Science and Technology of China (Nos. 2021YFB2501900, 2019YFE0100200 and 2019YFA0705703). We thank International Science Editing (http://www.internationalscienceediting.com) for editing this manuscript.

Appendix A. Supplementary data

Supplementary data to this article can be found online at https://doi.org/10.1016/j.cej.2022.139986.

References

[1] Y. Wang, Y. Wang, E. Hosono, K. Wang, H. Zhou, The design of a $LiFePO_4$/Carbon nanocomposite with a core–shell structure and its synthesis by an in situ polymerization restriction method, Angew. Chem. Int. Ed. 47 (39) (2008) 7461–7465. https://doi.org/10.1002/anie.200802539.

[2] R. Malik, A. Abdellahi, G. Ceder, A critical review of the Li insertion mechanisms in $LiFePO_4$ electrodes, J. Electrochem. Soc. 160 (5) (2013) A3179–A3197, https://doi.org/10.1149/2.029305jes.

[3] W.-J. Zhang, Structure and performance of $LiFePO_4$ cathode materials: a review, J. Power Sources 196 (6) (2011) 2962–2970. https://doi.org/10.1016/j.jpowsour.2010.11.113.

[4] A.K. Padhi, K.S. Nanjundaswamy, J.B. Goodenough, Phospho-olivines as positive-electrode materials for rechargeable lithium batteries, J. Electrochem. Soc. 144 (4) (1997) 1188–1194, https://doi.org/10.1149/1.1837571.

[5] T. Bashir, S.A. Ismail, Y. Song, R.M. Irfan, S. Yang, S. Zhou, J. Zhao, L. Gao, A review of the energy storage aspects of chemical elements for Lithium-ion based batteries, Energy Mater. 1 (2) (2021) 100019. https://doi.org/10.20517/energymater.2021.20.

[6] J. Li, Z.-F. Ma, Past and present of $LiFePO_4$: from fundamental research to industrial applications, Chem 5 (1) (2019) 3–6. https://doi.org/10.1016/j.chempr.2018.12.012.

[7] F. Zhou, K. Kang, T. Maxisch, G. Ceder, D. Morgan, The electronic structure and band gap of $LiFePO_4$ and $LiMnPO_4$, Solid State Commun. 132 (3) (2004) 181–186. https://doi.org/10.1016/j.ssc.2004.07.055.

[8] L. Yang, W. Deng, W. Xu, Y. Tian, A. Wang, B. Wang, G. Zou, H. Hou, W. Deng, X. Ji, Olivine $LiMn_xFe_{1-x}PO_4$ cathode materials for lithium ion batteries: restricted factors of rate performances, J. Mater. Chem. A 9 (25) (2021) 14214–14232, https://doi.org/10.1039/d1ta01526e.

[9] Y. Deng, C. Yang, K. Zou, X. Qin, Z. Zhao, G. Chen, Recent advances of Mn-rich $LiFe_{1-y}Mn_yPO_4$ ($0.5 \leq y < 1.0$) cathode materials for high energy density Lithium ion batteries, Adv. Energy Mater. 7 (13) (2017) 1601958, https://doi.org/10.1002/aenm.201601958.

[10] C. Liu, Z.G. Neale, G. Cao, Understanding electrochemical potentials of cathode materials in rechargeable batteries, Mater. Today 19 (2) (2016) 109–123. https://doi.org/10.1016/j.mattod.2015.10.009.

[11] A. Gutierrez, N.A. Benedek, A. Manthiram, Crystal-chemical guide for understanding redox energy variations of $M^{2+/3+}$ couples in polyanion cathodes for Lithium-ion batteries, Chem. Mater. 25 (20) (2013) 4010–4016, https://doi.org/10.1021/cm401949n.

[12] V. Aravindan, J. Gnanaraj, Y.-S. Lee, S. Madhavi, $LiMnPO_4$ – a next generation cathode material for lithium-ion batteries, J. Mater. Chem. A 1 (11) (2013) 3518–3539, https://doi.org/10.1039/C2TA01393B.

[13] C.L. Hu, H.H. Yi, F.X. Wang, S.Y. Xiao, Y.P. Wu, D. Wang, D.L. He, Boron doping at P-site to improve electrochemical performance of $LiMnPO_4$ as cathode for lithium ion battery, J. Power Sources 255 (2014) 355–359. https://doi.org/10.1016/j.jpowsour.2013.12.040.

[14] L.-E. Li, J. Liu, L. Chen, H. Xu, J. Yang, Y. Qian, Effect of different carbon sources on the electrochemical properties of rod-like $LiMnPO_4$–C nanocomposites, RSC Adv. 3 (19) (2013) 6847–6852, https://doi.org/10.1039/C3RA22862B.

[15] M. Yonemura, A. Yamada, Y. Takei, N. Sonoyama, R. Kanno, Comparative kinetic study of olivine Li_xMPO_4 (M=Fe, Mn), J. Electrochem. Soc. 151 (9) (2004) A1352, https://doi.org/10.1149/1.1773731.

[16] S.-I. Nishimura, G. Kobayashi, K. Ohoyama, R. Kanno, M. Yashima, A. Yamada, Experimental visualization of lithium diffusion in Li_xFePO_4, Nat. Mater. 7 (9) (2008) 707–711, https://doi.org/10.1038/nmat2251.

[17] K.M.Ø. Jensen, M. Christensen, H.P. Gunnlaugsson, N. Lock, E.D. Bøjesen, T. Proffen, B.B. Iversen, Defects in hydrothermally synthesized $LiFePO_4$ and $LiFe_{1-x}Mn_xPO_4$ cathode materials, Chem. Mater. 25 (11) (2013) 2282–2290, https://doi.org/10.1021/cm4008393.

[18] A. Yamada, Y. Kudo, K.-Y. Liu, Phase diagram of $Li_x(Mn_yFe_{1-y})PO_4$ ($0 \leq x, y \leq 1$), J. Electrochem. Soc. 148 (10) (2001), https://doi.org/10.1149/1.1401083.

[19] A. Yamada, S.-C. Chung, Crystal chemistry of the olivine-type $Li(Mn_yFe_{1-y})PO_4$ and $(Mn_yFe_{1-y})PO_4$ as possible 4 V cathode materials for lithium batteries, J. Electrochem. Soc. 148 (8) (2001) A960, https://doi.org/10.1149/1.1385377.

[20] A. Yamada, Y. Kudo, K.-Y. Liu, Reaction mechanism of the olivine-type $Li_x(Mn_{0.6}Fe_{0.4})PO_4$ ($0 \leq x \leq 1$), J. Electrochem. Soc. 148 (7) (2001) A747, https://doi.org/10.1149/1.1375167.

[21] J. Liu, X. Liu, T. Huang, A. Yu, Synthesis of nano-sized $LiMnPO_4$ and in situ carbon coating using a solvothermal method, J. Power Sources 229 (2013) 203–209. https://doi.org/10.1016/j.jpowsour.2012.11.093.

[22] A. Iadecola, A. Perea, L. Aldon, G. Aquilanti, L. Stievano, Li deinsertion mechanism and Jahn-Teller distortion in $LiFe_{0.75}Mn_{0.25}PO_4$: an operando X-ray absorption spectroscopy investigation, J. Phys. D: Appl. Phys. 50 (14) (2017), 144004, https://doi.org/10.1088/1361-6463/aa605c.

[23] R. Malik, F. Zhou, G. Ceder, Phase diagram and electrochemical properties of mixed olivines from first-principles calculations, Phys. Rev. B 79 (21) (2009), 214201, https://doi.org/10.1103/PhysRevB.79.214201.

[24] Y. Wang, Y. Wang, X. Liu, B. Zhu, F. Wang, Solvothermal synthesis of $LiFe_{1/3}Mn_{1/3}Co_{1/3}PO_4$ solid solution as lithium storage cathode materials, RSC Adv. 7 (24) (2017) 14354–14359, https://doi.org/10.1039/c7ra01396e.

[25] R. Wang, J. Zheng, X. Feng, G. Yao, H. Niu, Q. Liu, W. Chen, Highly [010]-oriented, gradient Co-doped $LiMnPO_4$ with enhanced cycling stability as cathode for Li-ion batteries, J. Solid State Electrochem. 24 (3) (2020) 511–519, https://doi.org/10.1007/s10008-019-04485-1.

[26] Y. Zhong, Z. Wu, J. Li, W. Xiang, X. Guo, BenHe Zhong, S. Sun, Synthesis of core-shell structured LiFe 0.5 Mn 0.3 Co 0.2 PO 4 @C with remarkable electrochemical performance as the cathode of a lithium-Ion battery, Chemelectrochem 2 (6) (2015) 896–902, https://doi.org/10.1002/celc.201402414.

[27] J. Yu, K.M. Rosso, J. Liu, Charge localization and transport in lithiated olivine phosphate materials, J. Phys. Chem. C 115 (50) (2011) 25001–25006, https://doi.org/10.1021/jp204188g.

[28] J. Lee, S.J. Pennycook, S.T. Pantelides, Simultaneous enhancement of electronic and Li^+ ion conductivity in $LiFePO_4$, Appl. Phys. Lett. 101 (3) (2012), 033901, https://doi.org/10.1063/1.4737212.

[29] Y. Mishima, T. Hojo, T. Nishio, H. Sadamura, N. Oyama, C. Moriyoshi, Y. Kuroiwa, MEM charge density study of olivine $LiMPO_4$ and MPO_4 (M = Mn, Fe) as cathode materials for Lithium-ion batteries, J. Phys. Chem. C 117 (6) (2013) 2608–2615, https://doi.org/10.1021/jp310075w.

[30] L.F.J. Piper, N.F. Quackenbush, S. Sallis, D.O. Scanlon, G.W. Watson, K.W. Nam, X. Q. Yang, K.E. Smith, F. Omenya, N.A. Chernova, M.S. Whittingham, Elucidating the nature of pseudo Jahn-Teller distortions in Li_xMnPO_4: combining density functional theory with soft and hard X-ray spectroscopy, J. Phys. Chem. C 117 (20) (2013) 10383–10396, https://doi.org/10.1021/jp3122374.

[31] S.K. Martha, J. Grinblat, O. Haik, E. Zinigrad, T. Drezen, J.H. Miners, I. Exnar, A. Kay, B. Markovsky, D. Aurbach, $LiMn_{0.8}Fe_{0.2}PO_4$: an advanced cathode material for rechargeable lithium batteries, Angew. Chem. Int. Ed. 48 (45) (2009) 8559–8563. https://doi.org/10.1002/anie.200903587.

[32] G.R. Gardiner, M.S. Islam, Anti-site defects and ion migration in the $LiFe_{0.5}Mn_{0.5}PO_4$ mixed-metal cathode material, Chem. Mater. 22 (3) (2010) 1242–1248, https://doi.org/10.1021/cm902720z.

[33] R. Malik, D. Burch, M. Bazant, G. Ceder, Particle size dependence of the ionic diffusivity, Nano Lett. 10 (10) (2010) 4123–4127, https://doi.org/10.1021/nl1023595.

[34] S.-M. Oh, S.-T. Myung, J.B. Park, B. Scrosati, K. Amine, Y.-K. Sun, Double-structured $LiMn_{0.85}Fe_{0.15}PO_4$ coordinated with $LiFePO_4$ for rechargeable lithium batteries, Angew. Chem. Int. Ed. 51 (8) (2012) 1853–1856. https://doi.org/10.1002/anie.201107394.

[35] L. Liao, H. Wang, H. Guo, P. Zhu, J. Xie, C. Jin, S. Zhang, G. Cao, T. Zhu, X. Zhao, Facile solvothermal synthesis of ultrathin $LiFe_xMn_{1-x}PO_4$ nanoplates as advanced cathodes with long cycle life and superior rate capability, J. Mater. Chem. A 3 (38) (2015) 19368–19375, https://doi.org/10.1039/C5TA05358G.

[36] R. von Hagen, H. Lorrmann, K.-C. Möller, S. Mathur, Electrospun $LiFe_{1-y}Mn_yPO_4$/C nanofiber composites as self-supporting cathodes in Li-ion batteries, Adv. Energy Mater. 2 (5) (2012) 553–559. https://doi.org/10.1002/aenm.201100534.

[37] S.-M. Oh, S.-T. Myung, Y.S. Choi, K.H. Oh, Y.-K. Sun, Co-precipitation synthesis of micro-sized spherical $LiMn_{0.5}Fe_{0.5}PO_4$ cathode material for lithium batteries, J. Mater. Chem. 21 (48) (2011) 19368–19374, https://doi.org/10.1039/C1JM13889H.

[38] L. Yang, Y. Xia, L. Qin, G. Yuan, B. Qiu, J. Shi, Z. Liu, Concentration-gradient $LiMn_{0.8}Fe_{0.2}PO_4$ cathode material for high performance lithium ion battery, J. Power Sources 304 (2016) 293–300. https://doi.org/10.1016/j.jpowsour.2015.11.037.

[39] L. Wang, X. He, W. Sun, J. Wang, Y. Li, S. Fan, Crystal orientation tuning of $LiFePO_4$ nanoplates for high rate lithium battery cathode materials, Nano Lett. 12 (11) (2012) 5632–5636, https://doi.org/10.1021/nl3027839.

[40] Y.-K. Hou, G.-L. Pan, Y.-Y. Sun, X.-P. Gao, $LiMn_{0.8}Fe_{0.2}PO_4$/Carbon nanospheres@graphene nanoribbons prepared by the biomineralization process as the cathode for Lithium-ion batteries, ACS Appl. Mater. Inter. 10 (19) (2018) 16500–16510, https://doi.org/10.1021/acsami.8b02736.

[41] T. Ruan, B. Wang, F. Wang, R. Song, F. Jin, Y. Zhou, D. Wang, S. Dou, Stabilizing the structure of $LiMn_{0.5}Fe_{0.5}PO_4$ via the formation of concentration-gradient hollow spheres with Fe-rich surfaces, Nanoscale 11 (9) (2019) 3933–3944, https://doi.org/10.1039/C8NR10224D.

[42] D. Ding, Y. Maeyoshi, M. Kubota, J. Wakasugi, K. Kanamura, H. Abe, Holey reduced graphene oxide/carbon nanotube/$LiMn_{0.7}Fe_{0.3}PO_4$ composite cathode for high-performance lithium batteries, J. Power Sources 449 (2020), 227553. https://doi.org/10.1016/j.jpowsour.2019.227553.

[43] X. Zhang, M. Hou, A.G. Tamirate, H. Zhu, C. Wang, Y. Xia, Carbon coated nano-sized $LiMn_{0.8}Fe_{0.2}PO_4$ porous microsphere cathode material for Li-ion batteries, J. Power Sources 448 (2020) 227438. https://doi.org/10.1016/j.jpowsour.2019.227438.

[44] H. Fang, E. Dai, B. Yang, Y. Yao, W. Ma, $LiMn_{0.8}Fe_{0.19}Mg_{0.01}PO_4$/C as a high performance cathode material for lithium ion batteries, J. Power Sources 204 (2012) 193–196. https://doi.org/10.1016/j.jpowsour.2011.12.046.

[45] X. Guo, M. Wang, X. Huang, P. Zhao, X. Liu, R. Che, Direct evidence of antisite defects in $LiFe_{0.5}Mn_{0.5}PO_4$ via atomic-level HAADF-EELS, J. Mater. Chem. A 1 (31) (2013) 8775–8781, https://doi.org/10.1039/C3TA11564J.

[46] A. Nytén, J.O. Thomas, A neutron powder diffraction study of $LiCo_xFe_{1-x}PO_4$ for x=0, 0.25, 0.40, 0.60 and 0.75, Solid State Ionics 177 (15) (2006) 1327–1330. https://doi.org/10.1016/j.ssi.2006.05.019.

[47] K. Dokko, S. Koizumi, H. Nakano, K. Kanamura, Particle morphology, crystal orientation, and electrochemical reactivity of $LiFePO_4$ synthesized by the hydrothermal method at 443 K, J. Mater. Chem. 17 (45) (2007) 4803, https://doi.org/10.1039/b711521k.

[48] J. Duan, G. Hu, Y. Cao, K. Du, Z. Peng, Synthesis of high-performance Fe–Mg-co-doped $LiMnPO_4$/C via a mechano-chemical liquid-phase activation technique, Ionics 22 (5) (2016) 609–619, https://doi.org/10.1007/s11581-015-1582-0.
[49] Y. Wang, H. Yang, C.-Y. Wu, J.-G. Duh, Facile and controllable one-pot synthesis of nickel-doped $LiMn_{0.8}Fe_{0.2}PO_4$ nanosheets as high performance cathode materials for lithium-ion batteries, J. Mater. Chem. A 5 (35) (2017) 18674–18683, https://doi.org/10.1039/C7TA05942F.
[50] Q.-Y. Huang, Z. Wu, J. Su, Y.-F. Long, X.-Y. Lv, Y.-X. Wen, Synthesis and electrochemical performance of Ti–Fe co-doped $LiMnPO_4$/C as cathode material for lithium-ion batteries, Ceramics Internat. 42 (9) (2016) 11348–11354. https://doi.org/10.1016/j.ceramint.2016.04.057.